

THE 3D ANALYSIS OF THE HELIOSPHERE USING INTERPLANETARY SCINTILLATION AND THOMSON-SCATTERING OBSERVATIONS

B. V. JACKSON

Center for Astrophysics and Space Sciences,

University of California, San Diego

9500 Gilman Dr. #0424, La Jolla,

CA 92093-0424, U.S.A.

bvjackson@ucsd.edu

<http://smei.ucsd.edu/>

<http://ips.ucsd.edu/>

Both interplanetary scintillation (IPS) and Thomson-scattering observations from the U.S. Air Force/NASA Solar Mass Ejection Imager (SMEI) allow a determination of velocity and density in the inner heliosphere and its forecast from remote-sensing heliospheric observations. Recent solar missions, such as *Hinode*, STEREO, and SDO, and resultant modeling analysis using these data enhance our ability to measure detailed aspects of specific solar events, including their outflow and three-dimensional structure. Current success in this 3D heliospheric endeavor includes the analysis of heliospheric structures that are also measured *in situ*: interplanetary Coronal Mass Ejections (CMEs), shocks, solar co-rotating structures, and the energy transport provided by solar wind plasma throughout the heliosphere. This report highlights a portion of the work on this multi-faceted topic.

1. Introduction

Beginning with observations from early coronagraphs (e.g., Jackson¹), a variety of techniques have been explored to provide the three-dimensional (3D) structure of the corona and heliosphere. When heliospheric imaging first began^{2,3} using interplanetary scintillation (IPS) techniques,⁴ it was clear that views of heliospheric structure over time could provide information about their 3D extent (e.g., Gapper *et al.*,² Hewish and Bravo,⁵ Behannon *et al.*⁶). The first of these techniques involved the use of different structure templates and the “by-eye” fitting of these according

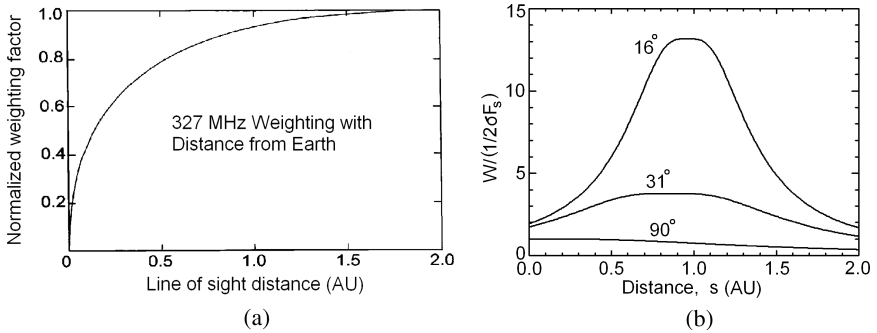


Fig. 1. LOS weighting functions. (a) The weak-scattering IPS weighting function at 327 MHz assuming a source size of 0.1 arc seconds (from Jackson *et al.*¹⁹). (b) The Thomson-scattering weight function. Three samples are given at angles from the Sun of 16°, 31°, and 90° (from Jackson and Hick²²).

to their line-of-sight (LOS) weighting response (Fig. 1). A second source of heliospheric remote sensing was introduced when it was proved that the same heliospheric structures registered a Thomson-scattering brightness response⁷ in the photometers⁸ of the *Helios* spacecraft.

IPS measurements have been used to track heliospheric structures outward from the Sun since the beginning of their use in heliospheric imaging. A recent review of many of these early techniques is given in Jackson *et al.*⁹ and references therein. In the late 1970's coronagraph techniques did not provide very clear images of Coronal Mass Ejections (CMEs). Ambiguities in IPS analysis were made using the 80 MHz Cambridge, England observations, and the comparisons of regions on the Sun, with *in-situ* measurements led Hewish and Bravo⁵ to describe most of the rapidly outward moving heliospheric structures observed as “coronal holes” to the consternation of many heliospheric physicists of that time. Later, measurements from more contemporary IPS arrays and data sets from the Large Angle Spectrographic COronagraphs (LASCO)¹⁰ flown on the Solar and Heliospheric Observatory (SOHO) spacecraft,¹¹ clearly showed that CMEs, or perhaps the turbulent shocked plasma behind some CMEs, constituted the majority of rapidly-moving transient features observed in the heliosphere.

The analysis of Solar Mass Ejection Imager (SMEI)^{12,13} data at the University of California, San Diego (UCSD) was developed to provide the same basic two-dimensional (2D) imaging input as IPS, but at a far higher temporal cadence, and precision in measuring density over

elongations (angular distances from the Sun) as great as 180° . Unlike IPS, the Thomson-scattering process is optically thin and directly related to heliospheric electron density by geometrical considerations alone.¹⁴ The originally-planned optical precision of SMEI observations is well-achieved in many sky locations most of the time,¹⁵ but the data are sometimes contaminated by aurorae near Earth above the polar-orbiting spacecraft.¹⁶ Thus SMEI performance is less than optimal at just those times of most interest for geoeffective studies and forecasts. Removing the auroral signatures from the SMEI images has been one of the most challenging aspects of these analyses to date. The LOS integration intrinsic to both IPS and Thomson-scattering observations precludes direct determination of the locations of outward-moving heliospheric structures, and thus a comparison with *in-situ* measurements requires additional more complicated analysis.

A technique was developed at the UCSD over the years¹⁷ aimed at formalizing the determination of the 3D extent of heliospheric structures by using the LOS response in either IPS (Fig. 1a) or Thomson-scattered light (Fig. 1b) data, and iteratively fitting these from only a few viewing locations, while making as few assumptions about the structures as possible.¹⁸ Over the years this iterative fitting became a more formal computational procedure, given that such a system was necessary to yield the greatest information about 3D structure from heliospheric data sets such as IPS, *Helios*, and SMEI, and that the procedure could do this from a single point in space (Fig. 2 and next paragraphs). For a review, see Jackson *et al.*⁹

The UCSD tomographic analysis technique explicitly takes into account the 3D extent of heliospheric structures, including the fact that the greatest contribution comes from material closest to the Sun, but without any

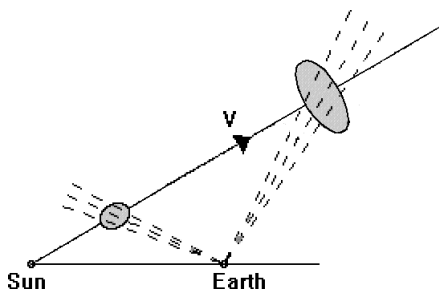


Fig. 2. Depiction of the perspective views from a single observing location (Earth) as material moves outward from the Sun (from Jackson *et al.*²³). This, and the LOS weighting change as the material flows outward, provide the necessary information about the shape of heliospheric structures.²⁴

explicit assumption about the distribution of velocity and density along their lines of sight. Thus, it reconstructs 3D solar wind structures from remote-sensing data gathered at a single location, such as are available from the IPS and SMEI observations. Developing this technique^{19–22} was necessary in order to tap the full potential of IPS and visible-light heliospheric imagers and to enable subsequent analysis as a predictive tool for scientific research and space-weather purposes.

Transients such as CMEs evolve on short time scales (hours to days). In the case of observations covering a wide range of solar elongations, heliospheric structures are seen from widely different perspectives as they move past Earth. This feature, which is absent from coronagraph and most other solar remote-sensing data, allows *time-dependent* 3D-reconstruction of transient structures. Presently, our time-dependent 3D-reconstruction incorporates a purely kinematic solar wind model. Given the velocity and density on an inner boundary (the “source surface”), a fully 3D solar wind model best fitting the observations can be derived by assuming radial outflow and enforcing conservation of mass and mass flux.¹⁹ Best fit is achieved iteratively. If the 3D solar wind model does not match the overall observations, the source surface values are suitably altered to minimize the deviations.

This technique is employed to successfully analyze CME-associated structures in an exploratory sense using IPS observations. A website is operated at: <http://ips.ucsd.edu> that has utilized this technique since the year 2000 and this provides data analysis in near real time. Also, the technique has been extended for use with visible-light brightness data from SMEI, and most recently for use with IPS archival data from Ootacamund (Ooty), India,^{25,26} to analyze the 6–8 November 2004 CME sequence.²⁷ See also Bisi *et al.*²⁸ and Hara *et al.*²⁹ for Solar-Terrestrial Environment Laboratory (STELab), Japan,³⁰ and SMEI data analysis of these events. The abundant velocity measurements from the Ooty single-site radio telescope provide truly outstanding data that match *in-situ* velocities made during this complex series of events. The analyses from STELab, SMEI, and Ooty have been compared successfully with *in-situ* measurements and examples of these based on IPS analysis are presented on the UCSD website. The 3D analysis and comparisons with near-Earth *in-situ* monitors and also with results from the Mars Global Surveyor,³¹ and with measurements made aboard the Solar-Terrestrial Relations Observatory (STEREO)³² spacecraft confirm that the IPS analysis provides accurate heliospheric density and velocity measurements throughout the heliosphere.

Here we report on just a few of the latest analyses accomplished using this 3D technique. Section 2 briefly describes the time-dependent tomographic analysis routines developed by our group at UCSD for fitting STELab IPS velocity and g -level data, and SMEI brightness data. Section 3 provides a set of recent observations and analyses. These are discussed briefly in Sec. 4. We conclude in Sec. 5.

2. 3D-Reconstruction Analysis

The mathematics of this technique are described in detail in Hick and Jackson,³³ and Jackson *et al.*,²⁴ and the reader can refer to these articles for more information than is given here. Also, computational aspects of the UCSD 3D-reconstruction program have been discussed in many other articles over the past decade.^{19,33,34} In early analyses it was assumed that the heliosphere co-rotates with the Sun. In more recent work^{20,21,35–39} this assumption has been relaxed. In the present case, LOS segments and their 3D weights are projected back in space and time to a solar wind inner boundary (a source surface) that is set at a given height (usually $15 R_S$) that lies below the closest approach of all lines of sight to the Sun. Each LOS is mapped from Earth and each segment of it is projected to the source surface taking into account the relevant velocities and interactions from the model that provides the solar wind outward motion (see Fig. 3).

In current analyses, the inversion process adjusts boundary conditions using a kinematic 3D solar wind model to best fit the observations and employing a least-squares fitting procedure. This minimizes the differences between modeled and observed SMEI brightness, or modeled and observed IPS g -value and velocity values, or a combination of these. As explained elsewhere,^{24,39} the mean solar wind Thomson-scattering signal from SMEI is difficult to distinguish from the very bright zodiacal light signal. Because of this, reconstructions based on SMEI data (unlike IPS g -level data) require that a mean ambient solar wind be included in the solar wind model as well as the observed Thomson-scattering brightness based on the average *in-situ* solar wind density at 1 AU.

A least-squares fitting program developed specifically for this type of analysis inverts the weighted, projected model values on the 2D inner-boundary source surface at different time steps, in order to provide solar wind model outflow parameters. These values are directly inverted on the source surface at the appropriate times to yield new solar wind parameters, and these latter are iteratively converged for each data set.

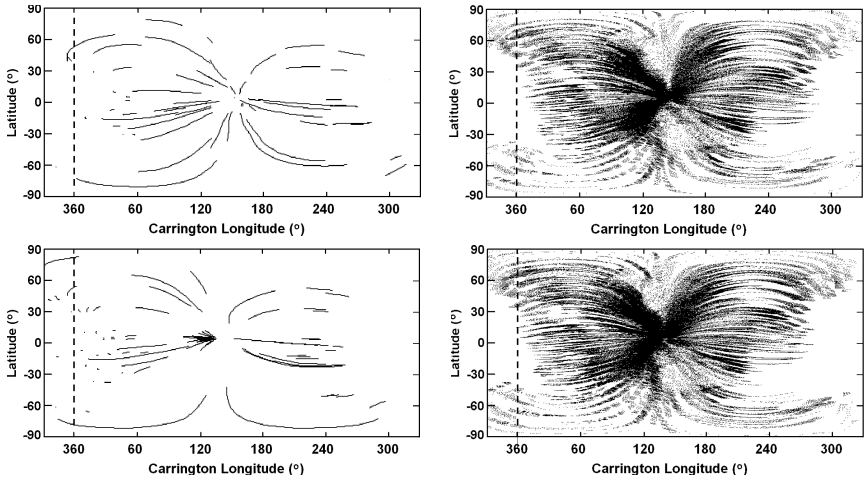


Fig. 3. Sample LOS segment mapping to the source surface over 360° (for one Carrington map at a given time). There is a slight displacement to the left over time from solar rotation; top to bottom. The mapping shows the coverage within the time interval from each segment. The Earth sub-point on these trace-back plots is at the approximate center. (left) Velocity LOS IPS projections from one day to another on 14 and 15 July 2000 (for time intervals of one day). (right) The Thomson-scattering LOS projections from SMEI from valid segments on $\sim 5^\circ$ image centers for two half-day time intervals using this same plot format during Carrington rotation 2068 (21 March–17 April 2008). There is far more spatial coverage from the SMEI images shown in these plots, and thus a far higher spatial and temporal resolution possible in SMEI analysis (from Jackson *et al.*²⁴).

In the fitting process, ratios of modeled-to-observed values and a modeled-to-observed χ^2 are monitored to indicate the rate of convergence for the interval studied. Velocity and density corrections to the 3D model are made separately. First, the inversion changes are made to previous velocity conditions on the inner boundary surface. Second, the 3D solar wind model is updated and new projected locations of each LOS point on the inner-boundary surface are determined. Third, inversion changes are made to previous density boundary conditions on the inner boundary surface. Finally, the 3D model is again updated with all the newest boundary values.

The inner-boundary Carrington maps of velocity and density are smoothed at every iterations using a 2D Gaussian spatial filter that incorporates equal-solar-surface areas, as well as a Gaussian temporal filter. Locations in the model that are not accessed by the above iterative procedure (and thus remain undetermined) are left blank in the final

result. For the analysis presented here, these blank places include sections of heliospheric volume on the opposite side of the Sun from Earth that cannot be accessed and thus not reconstructed with the resolutions of the 3D volume at the digital resolution used. For SMEI, this includes a large fraction of the region behind the Sun because the instrument does not view close to the solar surface. This blank volume is usually much smaller for the 327 MHz IPS data which can often view to within 11.5° of the Sun.

The reconstruction program generally converges to an unchanging model within a few iterations, but operates for nine iterations to guarantee convergence.¹⁹ For a typical rotation and the digital resolutions of the current SMEI data sets, the density and velocity iterations generally take about 15 minutes to process using a 2.4 GHz Intel[®] Core i7 computer. The IPS data sets normally take only a few minutes to process. Normally those IPS-velocity observations and SMEI-brightness lines of sight throughout the period that do not fit within a three-sigma limit of the mean ratio change ascribed at that location by the model (typically $\sim 1\%$ of the SMEI brightness or the IPS velocity line of sight) are discarded. This provides a safeguard by removing outliers which do not fit the model values. The program then operates for nine more iterations (18 in total). The solutions are insensitive to the initial model values and, after a few iterations, any residue of the initial values has disappeared. Tests¹⁹ have shown that the 3D-reconstruction of a set of artificial observations using a known 3D input successfully reproduces the input.

3. Recent Observations and Analysis

Examples of the 3D analysis procedure are presented below in four subsections: The first shows comparisons of velocity and density at Earth from the IPS data that have been verified by *in-situ* measurements; the second presents examples of our analysis that show both a CME and a co-rotating region using SMEI Thomson-scattering data compared with a current 3D-MHD model. The third gives measurements of a CME that was observed near the Sun in coronagraph observations and that was also measured *in situ* at the STEREO-B spacecraft situated 72° east of the Sun–Earth line; the fourth and final subsection describes a speculative recent analysis with tomography using IPS observations and the full SMEI data set. This latter example details a structure that was first observed in a coronagraph and then in the IPS and SMEI 3D-reconstructions, and that appears to be a manifestation of jets observed in *Hinode* data.

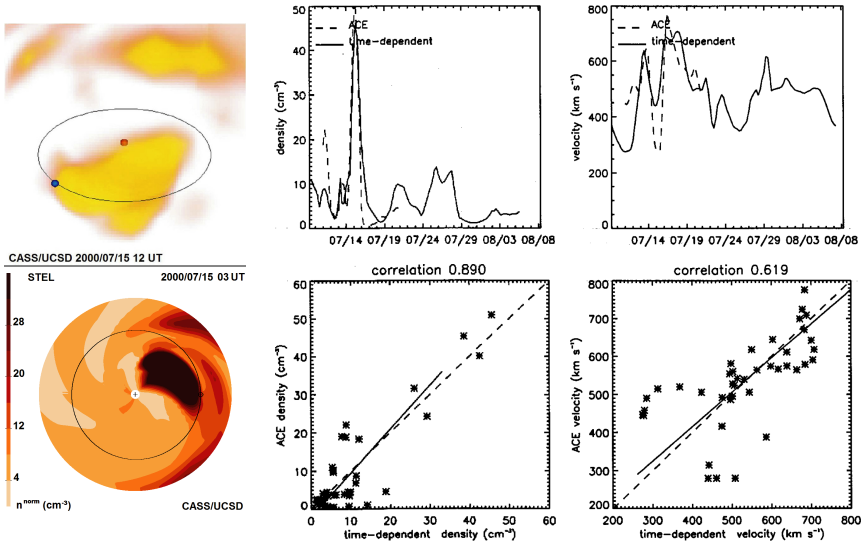


Fig. 4. Time-dependent reconstruction during Carrington rotation 1965 (10 July to 4 August 2000) using STELab IPS g -level data. (see Jackson *et al.*²¹). Upper Left: Density distribution as seen by an observer at 3 AU, 30° above the ecliptic, at the time indicated. The Sun, Earth, and Earth's orbit are indicated in the image. The main structure near Earth is associated with a halo CME (the “Bastille-Day” CME) observed by LASCO on 14 July 2000. The reconstruction has a resolution of $20^\circ \times 20^\circ$ in latitude and longitude, 0.25 AU in radial distance, and has a time cadence of one day. Lower Left: Elliptical cut from the Sun outward to 1.5 AU of the same CME. In this and the previous image an r^{-2} density fall-off has been removed from the volume to better view structure from near the Sun to farther away. Center: Time series and correlation of reconstructed density at Earth and measured proton density by the Advanced Composition Explorer (ACE) spacecraft. ACE observations are combined into 18-hour averages commensurate with the resolution of the time-dependent model. Correlation has been limited to data times within five days of the event. Right: Same for the reconstructed velocity and ACE velocity observations.

3.1. The 14 July 2000 (Bastille-Day) CME

The 3D time-dependent reconstruction technique was used to analyze CME-associated structures using IPS g -level and velocity observations. Figure 4 shows an example of the “Bastille-Day” CME of 14 July 2000.²¹ Gaussian filters were applied to the data sets to restrict structure size to larger than the digital resolution.^{35,39}

Here the dense structure reconstructed in the Bastille-Day CME event essentially traces the lower portion of a magnetic flux rope cylinder.^{40,41} The magnetic loop extent can only be inferred from its passage by Earth (using

Advanced Composition Explorer (ACE) and other near-Earth spacecraft *in-situ* observations), and by the Near Earth Asteroid Rendezvous (NEAR) spacecraft situated at ~ 1.76 AU nearly on the Sun–Earth line. This cylinder was a huge structure with the same approximate orientation as the reconstructed density. Thus, the 3D-reconstructed density for this feature mimics the flux rope cylinder to the east and west of the Sun derived from the magnetic analysis of data measured at the Earth and at the NEAR spacecraft.

3.2. The 26 April 2008 CME and co-rotating region

A simple kinematic solar wind model is presently the kernel of the UCSD 3D-reconstruction technique. At current resolutions, the kinematic modeling provides adequate 3D analysis near Earth. However, the physics behind this modeling becomes inadequate when either near the Sun or very distant from it, or when exploring shock processes. Numerical solar wind models based on the equations of magnetohydrodynamics (MHD) are currently the only self-consistent mathematical descriptions, capable of bridging many AU, from near the Sun to beyond Earth’s orbit. Although MHD provides only an approximation of actual plasma behavior, these models have successfully simulated many important space plasma processes. Some MHD algorithms are available from sources such as the NASA Goddard Community Coordinated Modeling Center (CCMC).

One such model ENLIL (Odstrcil *et al.*⁴²) is based on the ideal 3D MHD description, with two additional continuity equations for tracking the injected CME material and the magnetic field polarity (see Odstrcil and Pizzo⁴³). Odstrcil has used boundary conditions available from our iteratively-fit kinematic 3D-reconstructions to drive the time-dependent heliospheric ENLIL model.⁴⁴

The MHD modeling, adjusted to match *in-situ* parameters, agrees well with global 3D-reconstructions. With the addition of an input from measurements of observed near-solar CMEs, and a “cone model” approximation to these⁴⁵ (for example, see Fig. 5a), the 3D-MHD densities and kinematic model 3D-reconstruction densities agree reasonably^{46,47} with SMEI 3D-reconstructions (Fig. 5b). The MHD modeling in this example shows the timing of the ICME density response at the STEREO-B spacecraft, and the interaction between the co-rotating interacting region and the ICME. SMEI also shows both structures. This analysis using our 3D-reconstruction is described further in other articles,^{47–50} which also describes various other

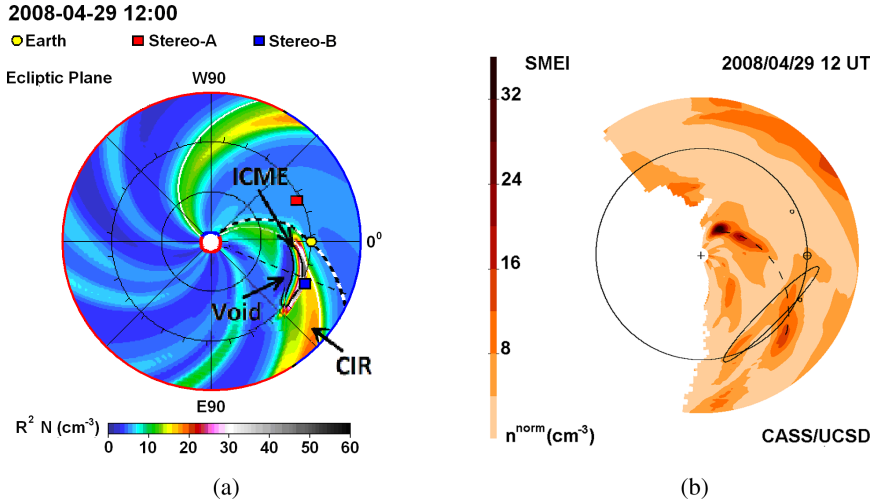


Fig. 5. Density comparison cuts in the ecliptic of the ENLIL 3D-MHD model that includes a cone model approximation, and the kinematic-model SMEI 3D-reconstruction of an ICME that arrives at STEREO-B on 29 April 2008 (from Jackson *et al.*⁴⁷). An r^{-2} density fall-off has been removed from both ecliptic cuts. (a) The ICME that reaches STEREO-B at this time is encircled by a black line. Additional features are annotated on the plot. A dashed line “streamline” connects Sun to Earth. (b) Density plot from the SMEI 3D-reconstruction. The ICME ecliptic response is enclosed by an ellipse; co-rotating structure about to reach STEREO-B is shown by a dashed line.

ICME modeling techniques^{51,52} that have been used to derive the 26 April 2008 ICME event and other CME shapes, as well as the solar wind density and velocity both in and out of the ecliptic.

Although we have highlighted the ENLIL 3D-MHD model in the above analysis, several other 3D-modeling efforts have compared well with past SMEI tomographic analysis. For the halo CMEs of 27–28 May 2003, comparisons between the Hakamada, Akasofu, and Fry, version 2 (HAF v2) kinematic model,⁵³ and the UCSD sky map of the event at 18 UT 29 May show very similar results. Also, in future efforts we could compare our results with other 3D-MHD modeling efforts such as the BATS-R-US code,⁵⁴ or with 3D-MHD codes by Wu *et al.*,⁵⁵ Feng *et al.*,⁵⁶ and Detman *et al.*⁵⁷ These 3D-MHD modeling procedures all begin by using solar magnetic fields to derive background solar wind parameters then, as in the case of ENLIL with its cone model input, some use energy inputs near the solar surface to propagate transient solar wind parameters. While these are all defensible forward-modeling procedures applying near-solar-surface inputs in a 3D-MHD model, they are used regularly only for larger CME events, and none match heliospheric remotely-sensed observations iteratively.

3.3. The January 2010 CME events

SMEI 3D-reconstructions have been applied for many CME event studies, but nowhere has this analysis been more productive than for the CME events of January 2010 which erupted near the solar east limb. This disturbance arrived *in situ* at the STEREO-B spacecraft at ~ 18 UT 20 January, and included a small density enhancement and a day-long magnetic field enhancement and rotation. The event passed the STEREO-B spacecraft at an average speed of $\sim 320 \text{ km s}^{-1}$. Using the SMEI 3D-reconstruction analysis technique and this speed we obtained an extremely good match with the density obtained at the time of the event in the data of STEREO-B, which was 72° east of the Sun–Earth line (Fig. 6). This *in-situ* fit during the event provides good assurance that the density structure reconstructed in 3D has the actual shape of the CME at the STEREO-B location. Figure 7a presents a 3D-reconstructed difference image of the CME when it was centered on the STEREO-B spacecraft at $\sim 55^\circ$ elongation to the east on the ecliptic. Figure 7b shows an ecliptic cut of the CME at the same time, and thereby provides a description of the shape of the CME density structure in the ecliptic.

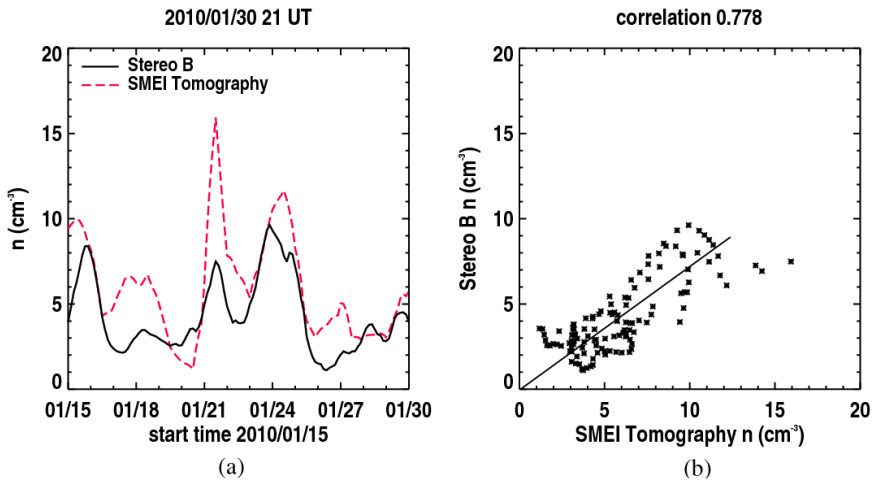


Fig. 6. (a) Density time series from the time-dependent 3D-reconstruction using SMEI brightness data compared with STEREO-B density data during the 15-day interval that the CME that passed STEREO on 20–21 January 2010 72° east of the Sun–Earth line. The dashed line time series is the reconstruction result, and the continuous line presents the *in-situ* measurements from STEREO-B. Density is presented from STEREO-B with a boxcar average of 0.5 day to approximately match the analysis from SMEI brightness. (b) Correlation between the two time-series over the interval shown.

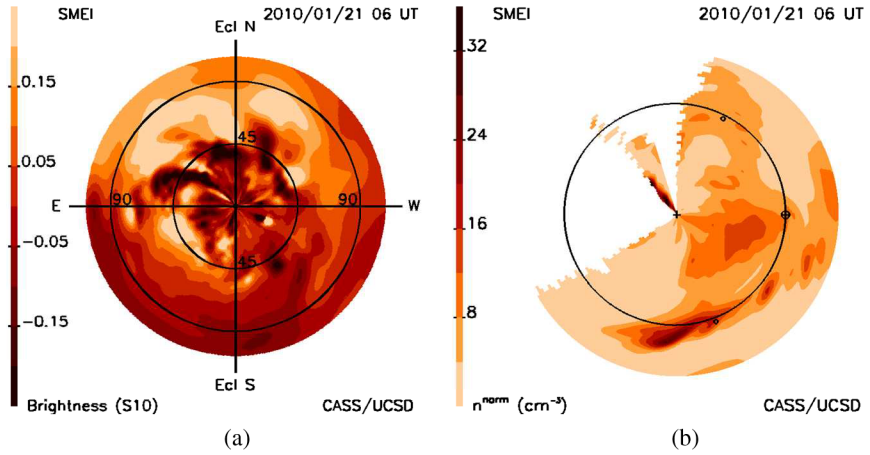


Fig. 7. (a) SMEI brightness difference image obtained from the 3D-reconstruction analysis by subtracting one volumetric data set 12 hours prior to the one indicated. In this “fisheye” presentation the Sun is centered with the largest elongation shown $\sim 110^\circ$. An r^{-2} density fall-off has been removed from the volumes to better show structures distant from the Sun with the same brightness near it. (b) Density ecliptic cut at the same time showing the CME structure as it passes STEREO-B during the event. The Earth is indicated on its orbit to the right of center with the locations of STEREO-A (above and right) and STEREO-B (below and right) shown as small circles near Earth’s orbit. The ecliptic density manifestation of the CME is an arch that follows the ecliptic over more than 60° to the east and west of STEREO-B. A second CME is nearing Earth at this same time.

The SMEI 3D analysis when extended back to the solar surface at a constant speed of 320 km s^{-1} can be used to show what the CME looked like earlier in the LASCO coronagraphs and these reconstructions can be compared with LASCO C3 images obtained at the appropriate time periods. The density enhancement present in the STEREO-B *in-situ* analysis on 21 January can be traced back directly to the CME event near the solar surface that erupted late on 14 January 2010 (Fig. 8). A later density enhancement that passed STEREO-B on 23–25 January that is also shown nearing Earth in the Fig. 7b ecliptic cut, can be traced back toward the solar surface at the same speed and is shown to have left the Sun on 17 January. The coronagraph brightness is decreased in its inner portion near the Sun due to vignetting of the inner field of the image. The SMEI pseudo coronagraph observations approximately match this vignettted brightness fall-off by providing a measurement of the inner corona brightness from data that had an r^{-2} density fall-off imposed on the volumetric analysis.

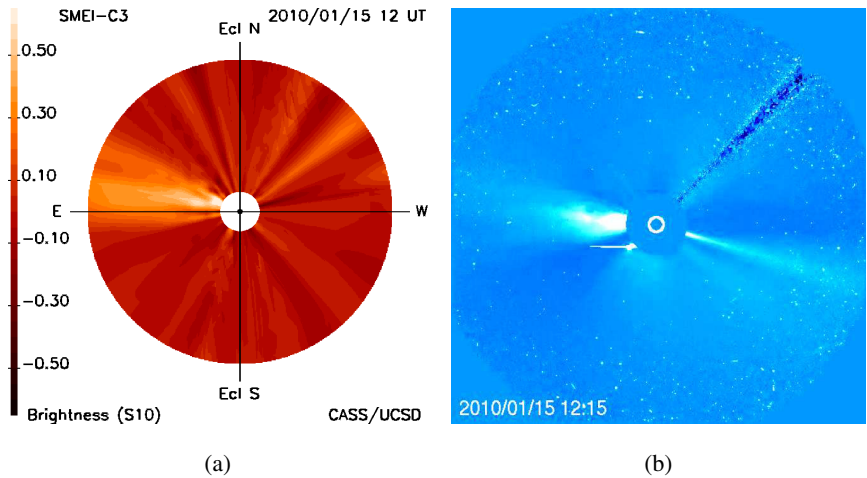


Fig. 8. (a) Brightness obtained using the 3D-density reconstruction from SMEI traced back to near the solar surface at the speed of 320 km s^{-1} , and presented as Thomson-scattering brightness viewed in LASCO C3 observations. The density has had an r^{-2} density fall-off applied, and is shown calibrated in S10 relative to the brightness the density would have at 1 AU. (b) A SOHO LASCO C3 image obtained showing a CME over the solar east limb that erupted from the solar surface late in the day on 14 January 2010.

The density enhancement associated with the magnetic cloud at STEREO-B is of great interest in this case because this enhancement was observed at the center of classical magnetic structure⁵⁸ associated with the CME, and can thus allow its orientation to be determined in 3D. We were indeed able to reconstruct this structure in 3D from the SMEI observations, determine its density orientation, and compare this with the 3D structure derived from *in-situ* magnetic field measurements as shown in these preliminary analyses.

3.4. The heliospheric response to jetting

Hinode (Solar B),⁵⁹ which was launched on 23 September 2006 to a polar Sun-synchronous orbit at about 600 km above the Earth, has a complement of three instruments that includes the X-Ray Telescope (XRT).^{60,61} With limited data downlink capability, the XRT has sometimes been run in campaign mode where images from the instrument from smaller area than the full solar disk are provided at a high temporal cadence. Figure 9 shows one image in a high-cadence (~ 1 min per image) sequence from XRT. Operated in conjunction with the Solar Optical Telescope (SOT)^{62–64} on board *Hinode*, these images, especially in polar regions, show solar

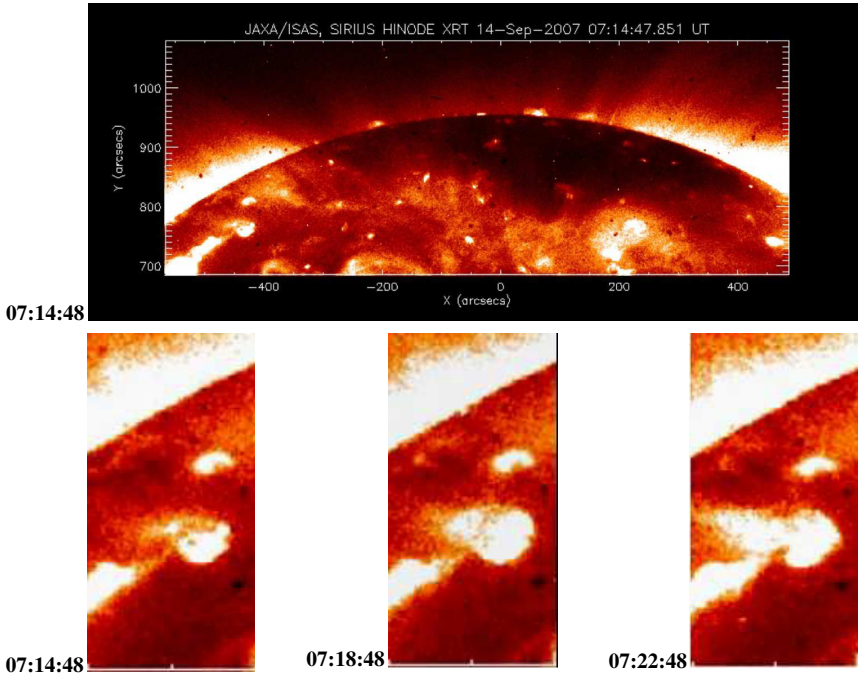


Fig. 9. *Hinode* XRT images using an Al_K filter showing the region that produces jets over the north solar pole. The base of the most dominant of these at this time (at 56°E, 57°N ecliptic relative to Earth) is shown enlarged in the three bottom panels. The jet ejecta response moves away from the Sun and eastward relative to its solar surface location.

jets and the locations of vertically-oriented flux tube structures⁶⁵ that are nearby. Figure 10 from Shimojo and Tsuneta⁶⁶ depicts the general structure surrounding the jetting region. Tsuneta *et al.*⁶⁵ describe the vertically-oriented flux tubes that have an average maximum field strength of 1.5 K Gauss, as “kG-patches”, and note that in any given polar region they all have the same sign, which is consistent with the polar magnetic field. If the flux tubes extend into interplanetary space, they have the possibility to serve as guide fields for X-ray jets, coronal plumes, and the fast solar wind.⁶⁶

Tsuneta *et al.*⁶⁵ remarked that the kG-patches probably fan out to provide all the open magnetic field in a coronal hole, and that these structures serve as the channels of the fast solar wind. However, Shimojo and Tsuneta⁶⁶ also concluded that since X-ray jets occur near only a small portion of the kG-patches, it is unlikely polar X-ray jets provide sufficient

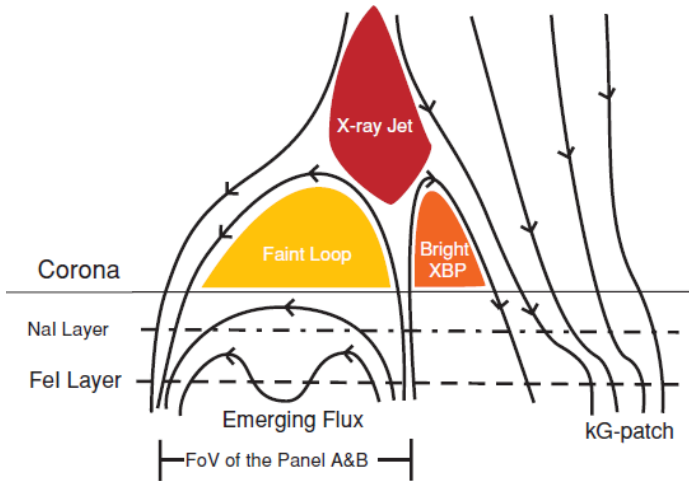


Fig. 10. The magnetic field configuration of the region around a jet as depicted by Shimojo and Tsuneta.⁵⁷ The X-ray jet is shown centered in the top of the image and moves outward adjacent to the kG-patch.

energy for the acceleration of the fast solar wind, and that the energy of the solar wind is most likely provided by weak activity surrounding the kG-patches.

Data sets from STELab (and SMEI) were used interactively at the CCMC in these 3D analyses⁶⁷ to provide quick comparisons with other data sets. Time-dependent 3D-reconstruction analyses from the IPS data sets have fairly low spatial and temporal resolutions (cadences of about one day, and latitudinal and longitudinal resolutions of $\sim 20^\circ$). Volumetric measurements feature a factor of four finer resolutions in order to smoothen up and provide somewhat higher spatial resolution and data cadence for the graphical displays at UCSD and the CCMC. In general these analyses do not show smoothly-flowing plasma, nor plasma that averages to the high polar speeds over the solar poles that are expected on the basis of *Ulysses in-situ* observations⁶⁸ (made during polar passes at >1.5 AU). An average tomographic measurement made over times greater than one day has allowed the group at STELab to split up the IPS measurements into those obtained close to the Sun and those farther away and to thereby discover a general acceleration term in the IPS velocity data set.⁶⁹

In a preliminary study of the solar jet response within the heliosphere, we chose a period for archival data analysis when *Hinode* observed the feature shown in Fig. 9. Within the period from 19 UT 5 September to

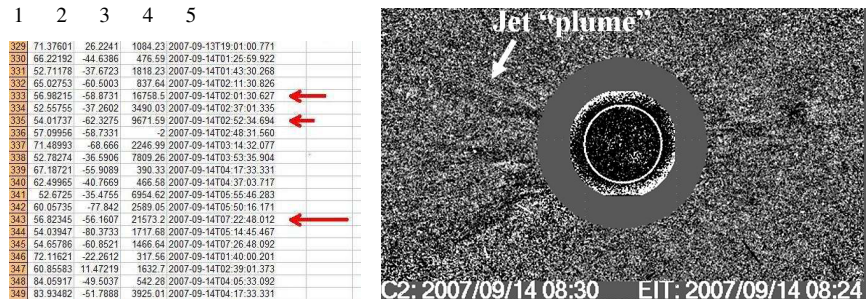


Fig. 11. (left) List of jet peak X-ray peak brightness energies on 14 September 2007 (column 4, event numbers 329 to 349) in DN s^{-1} from ~ 850 events observed in the *Hinode* XRT observations during a three-week interval (from Sako *et al.*⁷⁰). (right) The LASCO response for the brightest of these events #343 (shown as an enhancement to the north and a depletion to the south — arrow) in difference images.

08 UT 22 September, several particularly bright X-ray jets were observed on 14 September 2007 in the northern polar coronal hole. In a study of nearly 850 jets and their associated energy analysis from the X-ray brightening, over a three-week period, Sako *et al.*⁷⁰ determine approximate energy inputs for each event measured, and these, including the example in Fig. 9, are highlighted in a list from the *Hinode* data for 14 September 2007 (Fig. 11a). The columns in the table from 1–5 respectively list the event number, latitude, longitude, peak brightness, and time. Though difficult to discern except in animations of the LASCO images, these events were each observed individually in LASCO C2 difference images to have surface-projected onsets commensurate within minutes to the times at which they were observed as the jet peak brightness responses in *Hinode*. All were situated at approximately the same location on the solar surface, and the most energetic of these events provided the largest C2 response while the smallest correspondingly provided the least. The LASCO C2 observation shown (Fig. 11b) highlights the brightest of the X-ray events that occurred during this interval.

Figure 12 shows an IPS velocity ecliptic-cut coordinate plot from the CCMC interactive visualization at heliographic radius $r=0.3\text{ AU}$ (~ 70 solar radii). Although the volumetric data are available from the 3D-reconstructions at the CCMC from $r=15$ solar radii (3.75° elongation) out to 3.0 AU , we calculate that $r=0.3\text{ AU}$ is the approximate location of the greatest LOS weighting, and thus this is the heliographic height of greatest certainty in the 3D fit, especially for data measured over the

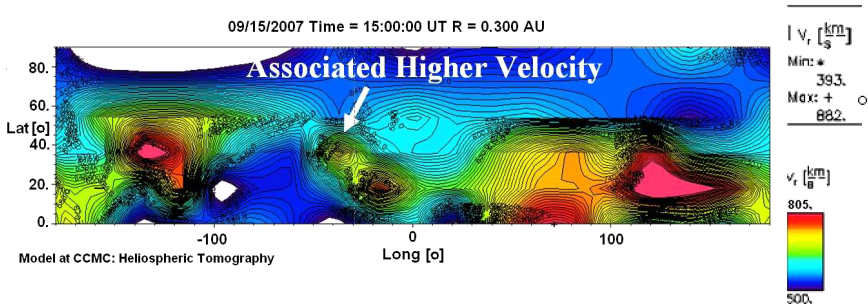


Fig. 12. An ecliptic-coordinate synoptic map presentation of IPS velocity volumetric data at a radial distance of 0.3 AU from the solar surface. The Sun–Earth line is centered at zero degrees longitude and latitude in the plot. A high-speed structure is marked by the arrow, and at this time is about 40°E, of the Sun–Earth line and 35°N latitude. Present a day earlier but as a smaller velocity enhancement, the feature increases to a maximum speed at this time and then diminishes. Contour intervals on the plot are placed from 500 to 800 km s^{-1} , at $\sim 10 \text{ km s}^{-1}$ interval to show only features in the generally faster-speed polar holes.

solar poles. The highlighted higher velocity region associated with the jet response has decreased in latitude by about 20° and is shifted somewhat westward from the jet solar surface location. The duration of the response which exceeds one day indicates that it is a composite of several responses to jetting activity observed in coronagraph observations at slightly earlier times.

In the SMEI analysis, the heliospheric response is clearer because of the higher data cadence and higher resolution available. By utilizing the full SMEI data set, some 4×10^6 LOS measurements over a Carrington rotation time interval, higher and more precise resolution analyses are provided for selected intervals than can be obtained normally (i.e., from our usual analysis at the CCMC or on the UCSD website at: <http://smei.ucsd.edu>). The jet response for this interval covered by Figs. 9, 11, and 12 is shown in the SMEI Thomson-scattering analysis where the observations from elongations of about 45° are back-projected to obtain the images shown in Fig. 13. These images show the SMEI observations near the solar surface presented as the C3 coronagraph would view the solar corona in white light. Although many radial structures are visible, enhancements at the correct position angles and times indicate that the SMEI instrument indeed viewed at least a remnant of the response observed in LASCO data at much larger distances from the Sun. That these structures correspond with the LASCO coronagraph observations implies that their 3D locations are

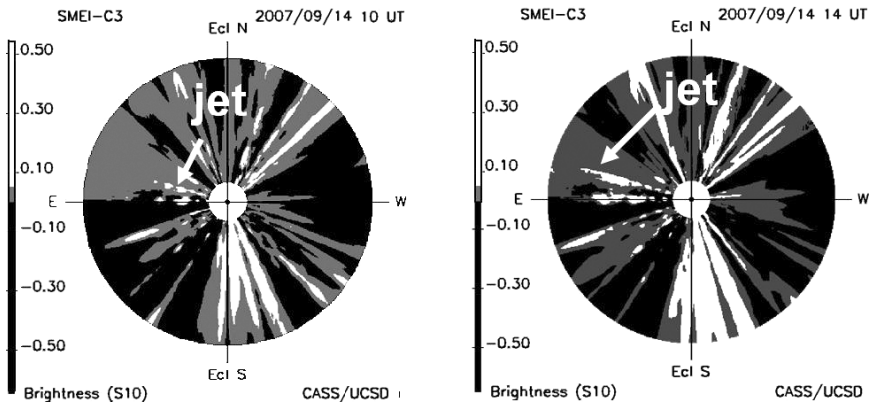


Fig. 13. Pseudo coronagraph images of the jet response shown in Figs. 9, 11, and 12 from the SMEI 3D-reconstruction analysis. The reconstructed back-projected image is as the C3 coronagraph would observe the sky in Thomson-scattered light. An r^{-2} density fall-off has been removed from the brightness response in order to mimic the coronagraph vignetting function.

properly known, and that they can be compared with their manifestations near the solar surface.

4. Discussion

The foregoing is a brief description of the exploratory type of 3D-reconstruction analysis that has been developed at UCSD over the last two decades. The current reconstruction analysis technique utilizes observations from a single location in space and assumes no *a-priori* knowledge of the heliospheric structure other than its LOS weighting and that the radial outward solar wind flow behaves kinematically, conserving mass and mass flux. The preceding gives examples of these analyses using both IPS and SMEI Thomson-scattering data.

Both of these data sets can be used in real time to forecast heliospheric 3D density and velocity in advance of its arrival at Earth and the inner planets. An article also submitted to this journal issue⁷¹ gives a more comprehensive account of the analysis technique used in IPS forecasting, and of the currently operating website, and details how this technique can be used in real time with the STELab system. Between the time this article was first conceived and its submission, the U.S. Air Force decided to stow the SMEI instrument, which is on board the Coriolis spacecraft, (on 28 September 2011), to save data access costs and civil-servant salaries during

a period of austerity in the U.S. Thus, for the foreseeable future there can only be access to SMEI archival data to support 3D analysis at UCSD, the CCMC, and at Nagoya, Japan.

5. Conclusion

Analysis of data from IPS systems have provided heliospheric results for over five decades; presently this science has advanced to the point of yielding precise global measurements over much of the inner heliosphere. This in turn has spawned heliospheric imaging systems, of which SMEI was a prototype, for more advanced instruments on proposed NASA and ESA spacecraft. Current analyses that explore the 3D structure with most planned spaceborne instruments do not have the maturity of IPS, and generally go only so far as to look at time sequences of 2D images or at 3D stereographic approximations of known structure shapes. Such essentially 2D image analyses often provide a good-enough story for these current rudimentary comparisons; however, full 3D analysis can be obtained after careful instrument calibration and thorough background noise elimination using Thomson-scattering results. Eventually, the requirement for analyses that match most aspects of detailed *in-situ* measurements globally will compel further development of more precise systems. For more details and to look into the research currently presented using these global exploratory 3D-reconstructions, the reader is referred to the many journal articles cited here.

Acknowledgments

I wish to thank the many colleagues who contributed to this work and for allowing it to be presented as a Distinguished Lecture for the Solar-Terrestrial Section of the AOGS. At UCSD these colleagues are P.P. Hick, A. Buffington and J.M. Clover. Special thanks are due M. Kojima and M. Tokumaru for making available IPS data for these analyses under the auspices of a joint CASS/UCSD-STELab cooperative agreement. Additional thanks are due M. Shimojo and M. Sako who have furnished data from *Hinode* for use in the jet response analysis. SMEI was designed and constructed by a team of scientists and engineers from the University of California, San Diego, the U.S. Air Force Research Laboratory, Boston College, Boston University, and the University of Birmingham, U.K. The work of B.V. Jackson, and colleagues at the University of California,

San Diego was supported by NSF grants ATM-0852246 and AGS-1053766, and NASA grant NNX11AB50G and AFOSR grant 11NE043.

References

1. B. V. Jackson, A coronal hole equatorial extension and its relation to a high speed solar wind stream, *Topical Conference on Solar and Interplanetary Physics*, Tucson, Arizona, 12–15 January, 1977, pp. 7–9.
2. G. R. Gapper, A. Hewish, A. Purvis and P. J. Duffet-Smith, *Nature* **296** (1982) 633–636.
3. B. V. Jackson, IPS Observations of the 14 August, 1979 Mass Ejection Transient, *Proc. of the Maymooth, Ireland Symposium on Solar/Interplanetary Intervals*, 1982, pp. 169–173.
4. Z. Houminer, *Nature Phys. Sci.* **231** (1971) 165–167.
5. A. Hewish and S. Bravo, *Solar Phys.* **106** (1986) 185–200.
6. K. W. Behannon, L. F. Burlaga and A. Hewish, *J. Geophys. Res.* **96** (1991) 21,213–21,225.
7. I. Richter, C. Leinert and B. Planck, *Astron. Astrophys.* **110** (1982) 115–120.
8. C. Leinert, H. Link, E. Pitz, N. Salm and D. Knuppelberg, *Raumfahrt forschung* **19** (1975) 264–267.
9. B. V. Jackson, P. P. Hick, A. Buffington, M. M. Bisi, J. M. Clover, M. Tokumaru, M. Kojima and K. Fujiki, *J. Atmospheric and Solar-Terrestrial Phys.* **73** (2011) 1–9.
10. G. E. Brueckner, R. A. Howard, M. J. Koomen, C. M. Korendyke, D. J. Michels, J. D. Moses, D. G. Socker, K. P. Dere, P. L. Lamy, A. Llebaria, M. V. Bout, R. Schwenn, G. M. Simnett, D. K. Bedford and C. J. Eyles, *Solar Phys.* **162** (1995) 357–402.
11. V. Domingo, B. Fleck and A. I. Poland, *Space Sci. Rev.* **72** (1995) 81–84.
12. C. J. Eyles, G. M. Simnett, M. P. Cooke, B. V. Jackson, A. Buffington, P. P. Hick, N. R. Waltham, J. M. King, P. A. Anderson and P. E. Holladay, *Solar Phys.* **217** (2003) 319–347.
13. B. V. Jackson, A. Buffington, P. P. Hick, R. C. Altrock, S. Figueroa, P. Holladay, J. C. Johnston, S. W. Kahler, J. Mozer, S. Price, R. R. Radick, R. Sagalyn, D. Sinclair, G. M. Simnett, C. J. Eyles, M. P. Cooke, S. J. Tappin, T. Kuchar, D. Mizuno, D. F. Webb, P. Anderson, S. L. Keil, R. Gold and N. R. Waltham, *Solar Phys.* **225** (2004) 177–207.
14. D. E. Billings, *A Guide to the Solar Corona* (Academic, New York, 1966) 150.
15. A. Buffington, D. L. Band, B. V. Jackson, P. P. Hick and A. C. Smith, *Astrophys. J.* **637** (2006) 880–888.
16. D. R. Mizuno, A. Buffington, M. P. Cooke, C. J. Eyles, P. P. Hick, P. E. Holladay, B. V. Jackson, J. C. Johnston, T. A. Kuchar, J. M. Mozer, S. D. Price, R. R. Radick, G. M. Simnett, D. Sinclair and D. F. Webb, *J. Geophys. Res.* **110** (2005) A07230.
17. B. V. Jackson, B. Rompolt and Z. Svestka, *Solar Phys.* **115** (1988) 327–343.
18. B. V. Jackson and H. R. Froehling, *Astron. Astrophys.* **299** (1995) 885–892.

19. B. V. Jackson, P. L. Hick, M. Kojima and A. Yokobe, *J. Geophys. Res.* **103** (1998) 12,049–12,067.
20. B. V. Jackson, A. Buffington and P. P. Hick, A heliospheric imager for solar orbiter, *Proc. of Solar Encounter: The First Solar Orbiter Workshop*, Puerto de la Cruz, Tenerife, Spain, 14–18 May, 2001, pp. 251–256.
21. B. V. Jackson, P. P. Hick, A. Buffington, M. Kojima, M. Tokumaru, K. Fujiki, T. Ohmi and M. Yamashita, Time-dependent tomography of heliospheric features using interplanetary scintillation (IPS) remote sensing observations, *CP679, Solar Wind Ten: Proceedings of the Tenth International Solar Wind Conference*, eds. M. Velli, R. Bruno and F. Malara, 2002, pp. 75–78.
22. B. V. Jackson and P. P. Hick, *Solar Phys.* **211** (2002) 345–356.
23. B. V. Jackson, A. Buffington, P. P. Hick, M. M. Bisi and J. M. Clover, *Solar Phys.* **265** (2010) 257–275.
24. B. V. Jackson, P. P. Hick, A. Buffington, M. M. Bisi, J. M. Clover and M. Tokumaru, *Adv. in Geosciences* **21** (2008) 339–366.
25. P. K. Manoharan, Study of the solar wind using single-station interplanetary scintillation, PhD thesis, University of Bombay, 1991, pp. 53–95.
26. P. K. Manoharan, *Solar Phys.* **265** (2010) 137–157.
27. M. M. Bisi, B. V. Jackson, J. M. Clover, P. K. Manoharan, M. Tokumaru, P. P. Hick, and A. Buffington, *Annales Geophysicae* **27** (2009) 4479–4489.
28. M. M. Bisi, R. A. Fallows, P. K. Manoharan, G. D. Dorrian, B. V. Jackson, J. M. Clover, P. P. Hick, A. Buffington, and A. R. Breen, *Adv. in Geosciences* **21** (2008) 33–49.
29. L. K. Hara, N. U. Crooker, C. H. Mandrini, L. van Driel-Gesztelyi, S. Dasso, J. Wang, H. Elliott, G. Attrill, B. V. Jackson, and M. M. Bisi, *Solar Phys.* **244** (2008) 95–114.
30. M. Kojima and T. Kakinuma, *J. Geophys. Res.* **92** (1987) 7269–7279.
31. B. V. Jackson, J. A. Boyer, P. P. Hick, A. Buffington, M. M. Bisi, and D. H. Crider, *Solar Phys.* **241** (2007) 385–396.
32. M. M. Bisi, B. V. Jackson, A. Buffington, J. M. Clover, P. P. Hick and M. Tokumaru, *Solar Phys.* **256** (2009) 201–217.
33. P. P. Hick and B. V. Jackson, Heliospheric tomography: an algorithm for the reconstruction of the 3D solar wind from remote sensing observations, *Proc. SPIE 5171*, 2004, pp. 287–297.
34. M. Kojima, M. Tokumaru, H. Watanabe, A. Yokobe, K. Asai, B. V. Jackson and P. L. Hick, *J. Geophys. Res.* **103** (1998) 1981–1989.
35. B. V. Jackson and P. P. Hick, Three-dimensional tomography of interplanetary disturbances, *Solar and Space Weather Radiophysics, Current Status and Future Developments (Astrophysics and Space Science Library, 315)*, eds. D. E. Gary and C. U. Keller, **315** (Kluwer Academic Publ., Dordrecht, The Netherlands, 2005) 355–386.
36. B. V. Jackson, A. Buffington, P. P. Hick, X. Wang and D. Webb, *J. Geophys. Res.* **111** (2006) A04S91.
37. B. V. Jackson, P. P. Hick, A. Buffington, M. M. Bisi, M. Kojima and M. Tokumaru, *Astronomical and Astrophysical Transactions* **26**(6) (2007) 477–487.

38. M. M. Bisi, B. V. Jackson, P. P. Hick, A. Buffington and J. M. Clover, *J. Geophys. Res. — Space Physics Special Edition — Geomagnetic Storms of Solar Cycle 23* **113** (2008) A00A11.
39. B. V. Jackson, M. M. Bisi, P. P. Hick, A. Buffington, J. M. Clover and W. Sun, *J. Geophys. Res.* **113** (2008) A00A15.
40. T. Mulligan, C. T. Russell, B. J. Anderson and M. H. Acuna, *Geophys. Res. Letts.* **28** (2001) 4417–4420.
41. M. Tokumaru, M. Kojima, K. Fujiki, M. Yamashita and A. Yokobe, *J. Geophys. Res.* **108**(A5) (2003) 1220.
42. D. Odstrcil, J. A. Linker, R. Lionello, Z. Mikic, P. Riley, V. J. Pizzo, and J. G. Luhmann, *J. Geophys. Res.* **107**(A12) (2002) SSH14-1-11.
43. D. Odstrcil and V. J. Pizzo, *J. Geophys. Res.* **104** (1999) 483–492.
44. D. Odstrcil, V. J. Pizzo, C. N. Arge, M. M. Bisi, P. P. Hick, B. V. Jackson, S. A. Ledvina, J. G. Luhmann, J. A. Linker, Z. Mikic, and P. Riley (2008), Numerical Simulations of Solar Wind Disturbances by Coupled Models, *ASP Conference Series Proceedings*, **385**, 2008, pp. 167–173.
45. J. G. Luhmann, S. A. Ledvina, D. Odstrcil, M. J. Owens, X.-P. Zhao, Y. Liu and P. Riley, *Adv. in Space Res.* **46**(1) (2010) 1–21.
46. D. Odstrcil, C. N. Arge, A. Rasca, A. Thernisien and H. Xie, Simulation of heliospheric disturbances initialized by various fitting techniques, NOAA Space Weather Workshop Boulder, CO, 27–30 April, 2010.
47. B. V. Jackson, A. Buffington, P. P. Hick, J. M. Clover, M. M. Bisi and D. F. Webb, *Astrophys. J.* **724** (2010) 829–834.
48. M. Bisi, B. Jackson, J. M. Clover, M. Tokumaru, A. Buffington, P. Hick and K. Fujiki, Coronal Mass Ejections in the Declining and Minimum Phase between Solar Cycles 23 and 24, *Eos Trans. AGU*, 14–18 December, 2009, Fall Meeting Suppl., Abstract SH43A-08, p. 374.
49. D. F. Webb, A. B. Galvin, N. Gopalswamy, T. A. Howard, A. A. Reinard, B. Jackson, and C. Davis, The 26 April 2008 CME; a Case Study Tracking a CME into the Heliosphere, *Eos Trans. AGU*, 14–18 December, 2009, Fall Meeting Suppl., Abstract SH41A-1640, p. 319.
50. B. V. Jackson, P. P. Hick, A. Buffington, J. M. Clover, D. B. Reisenfeld and T. R. Abell, 3-D Reconstruction of the Inner Heliosphere: A Global Solar Wind Boundary from Remote-Sensing Data, Invited presentation to the ninth annual CSPAR Conference, Maui, Hawaii, 14–19 March, 2010.
51. B. E. Wood and R. A. Howard, *Astrophys. J.* **702** (2009) 901–910.
52. N. Lugaz, J. N. Hernandez-Charpak, I. I. Roussev, C. J. Davis, A. Vourlidas and J. A. Davies, *Astrophys. J.* **715** (2010) 493–499.
53. W. Sun, C. S. Deehr, M. Dryer, C. D. Fry, Z. K. Smith and S.-I. Akasofu, *Space Weather* **6** (2008) S03006.
54. G. Toth, D. L. De Zeeuw, T. I. Gombosi and K. G. Powell, *J. Comp. Phys.*, **217** (2006) 722–758.
55. C. C. Wu, C. D. Fry, S. T. Wu, M. Dryer and K. Liou, *J. Geophys. Res.* **112** (2007) A09104.
56. X. Feng, L. Yang, C. Xiang, S. T. Wu, Y. Zhou and D. K. Zhong, *Astrophys. J.* **723**(1) (2010) 300–319.

57. T. R. Detman, D. S. Intriligator, M. Dryer, W. Sun, C. S. Deehr and J. Intriligator, *J. Geophys. Res.* **116** (2011) A03105.
58. L. F. Burlaga, *J. Geophys. Res.* **93** (1988) 7217–7224.
59. T. Kosugi, K. Matsuzaki, T. Sakao, T. Shimizu, T. Sone, S. Tachikawa, T. Hashimoto, K. Minesugi, A. Ohnishi and T. Yamada, *et al.*, *Solar Phys.* **243** (2007) 3–17.
60. L. Golub, E. DeLuca, G. Austin, J. Bookbinder, D. Caldwell, P. Cheimets, J. Cirtain, M. Cosmo, P. Reid and A. Sette, *et al.*, *Solar Phys.* **243** (2007) 63–86.
61. R. Kano, T. Sakao, H. Hara, S. Tsuneta, S. Matsuzaki, K. Kumagai, M. Shimojo, K. Minesugi, K. Shibasaki and E. E. DeLuca, *et al.*, *Solar Phys.* **249** (2008) 263–279.
62. S. Tsuneta, K. Ichimoto, Y. Katsukawa, S. Nagata, M. Otsubo, T. Shimizu, Y. Suematsu, M. Nakagiri, M. Noguchi, and T. Tarbell, *et al.*, *Solar Phys.* **249** (2008) 167–196.
63. Y. Suematsu, S. Tsuneta, K. Ichimoto, T. Shimizu, M. Otsubo, Y. Katsukawa, M. Nakagiri, M. Noguchi, T. Tamura and Y. Kato, *et al.*, *Solar Phys.* **249** (2008) 197–220.
64. K. Ichimoto, B. Lites, D. Elmore, Y. Suematsu, S. Tsuneta, Y. Katsukawa, T. Shimizu, R. Shine, T. Tarbell and A. Title, *et al.*, *Solar Phys.* **249** (2008) 233–261.
65. S. Tsuneta, K. Ichimoto, Y. Katsukawa, B. W. Lites, K. Matsuzaki, S. Nagata, *et al.*, *Astrophys. J.* **688** (2008) 1374–1381.
66. M. Shimojo and S. Tsuneta, *Astrophys. J. Letts.* **706** (2009) L145–L149.
67. P. MacNiece, Solar and Heliospheric Modeling at the CCMC, SHINE 06 Workshop, Midway, UT, 31 July–4 Aug, 2006.
68. D. J. McComas, B. L. Barraclough, H. O. Funsten, J. T. Gosling, E. Santiago-Muñoz, R. M. Skoug, B. E. Goldstein, M. Neugebauer, P. Riley and A. Balogh, *J. Geophys. Res.* **105**(A5) (2000) 10,419–10,433.
69. M. Kojima, A. R. Breen, K. Fujiki, K. Hayashi, T. Ohmi and M. Tokumaru, *J. Geophys. Res.* **109** (2004) A04103.
70. M. Sako, M. Shimojo and T. Kitabayashi, Statistical study of the polar X-ray jets, 38th COSPAR Scientific Assembly, 2010, E21-0018-10.
71. B. V. Jackson, P. P. Hick, A. Buffington, J. M. Clover and M. Tokumaru, *Adv. in Geosciences*, (in press 2012).